PCCP

PAPER

Cite this: *Phys. Chem. Chem. Phys.*, 2018, **20**, 24434

Measurement of the surface hydrophobicity of engineered nanoparticles using an atomic force microscope†

Wanyi Fu and Wen Zhang *

Received 24th July 2018,
Accepted 31st August 2018

DOI: 10.1039/c8cp04676j

rsc.li/pccp

Determination of the surface hydrophobicity or wettability of nanomaterials and nanoparticles (NPs) is often challenged by the heterogeneous properties of NPs that vary with particle size, shape, surface charge, aggregation states, and surface sorption or coating. This study first summarized inherent limitations of the water contact angle, octanol–water partition coefficient (K_{ow}) and surface adsorption of probe molecules in probing nanomaterial hydrophobicity. Then, we demonstrated the principle of a scanning probe method based on atomic force microscopy (AFM) for the local surface hydrophobicity measurement. Specifically, we measured the adhesion forces between functionalized AFM tips and self-assembled monolayers (SAMs) to establish a linear relationship between the adhesion forces and water contact angles based on the continuum thermodynamic approach (CTA). This relationship was used to determine the local surface hydrophobicity of seven different NPs (*i.e.*, TiO_2, ZnO, SiO_2, CuO, CeO_2, α-Fe_2O_3, and Ag), which agreed well with bulk contact angles of these NPs. Some discrepancies were observed for Fe_2O_3, CeO_2 and SiO_2 NPs, probably because of surface hydration and roughness effects. Moreover, the solution pH and ionic strength had negligible effects on the adhesion forces between the AFM tip and MWCNTs or C_{60}, indicating that the hydrophobicity of carbonaceous nanomaterials is not influenced by pH or ionic strength (IS). By contrast, natural organic matter (NOM) appreciably decreased the hydrophobicity of MWCNTs and C_{60} due to surface coating of hydrophilic NOM. This scanning probe method has been proved to be reliable and robust toward the accurate measurement of the nanoscale hydrophobicity of individual NPs or nanomaterials in liquid environments.

1. Introduction

Extensive use of anthropogenic nanomaterials in industry and consumer products has increased the likelihood of their exposure to the natural environment. Consequently, the concern over the potential toxicity of nanoparticles (NPs) to the environment and human health is indisputably mounting. Extensive research has demonstrated that metal oxide NPs (*e.g.*, TiO_2, ZnO, and Fe_2O_3) can disrupt cell membrane surfaces,[1–3] and induce cytotoxicity,[4,5] cell penetration,[6] and uptake by gastrointestinal cell lines.[1,7,8] Effective characterization of the physicochemical properties of engineered nanoparticles (ENPs) is critical for understanding their potential fate, transport, and bioavailability.[9,10] Accurate measurement of the interfacial properties of ENPs is also important for the development of functional nanomaterials for diverse environmental or industrial applications.

1.1. Impact of hydrophobicity on the fate and transport of NPs in an aqueous environment

Among numerous nanomaterial properties (*e.g.*, size, shape, surface charge, and coating), surface hydrophobicity or hydrophilicity (also known as wettability) has pivotal impacts on their stability, fate, transport, and interfacial interactions such as inter-particle repulsion or attraction. For example, water molecules adhere to hydrophilic NPs and form steric layers on their surfaces, which may prevent other particles or molecules from approaching or interacting. Alternatively, if the relative affinity of water molecules toward the particle surface is lower than that between NPs themselves, rapid attraction and aggregation of NPs will occur, which is termed as hydrophobic attraction or the hydrophobic effect.[11] Therefore, surface hydrophobicity affects particle stability and interfacial processes (*e.g.*, molecular adsorption).

Hydrophobic NPs may preferentially partition into hydrophobic regions of the cell membrane and result in higher potential of accumulation and penetration across the cells.[12,13] For example, hydrophobic nanomaterials like carbon nanotubes or graphene have a tendency to partition into the lipid bilayer of the cell membrane, which strongly affects the biological

John A. Reif, Jr. Department of Civil and Environmental Engineering, New Jersey Institute of Technology, 323 Martin Luther King Blvd., Newark, New Jersey 07102, USA. E-mail: wen.zhang@njit.edu; Fax: +1 973 596-5790; Tel: +1 973 596-5520

† Electronic supplementary information (ESI) available. See DOI: 10.1039/c8cp04676j

toxicity of NPs.[14,15] Therefore, developing suitable characterization methods for probing surface hydrophobicity at the nanoscale is indispensable for the comprehensive understanding of environmental processes and cell interactions of NPs.

1.2. Factors affecting surface hydrophobicity

Nanomaterial hydrophobicity is difficult to assess due to dynamic changes and processes (*e.g.*, protein sorption and corona formation) of nanomaterials upon their release into the environment. For example, transition-metal oxides, such as TiO_2 and ZnO, are well-known to exhibit photo-induced hydrophilicity under UV irradiation.[16,17] The hematite (α-Fe_2O_3) surface also demonstrated switchable hydrophobicity from superhydrophobicity to superhydrophilicity and *vice versa* with UV_{254} irradiation and dark storage.[18] Moreover, a hydrophobic shift could also be ascribed to the adsorption of proteins (*e.g.*, albumin and fibronectin) and natural organic matter (NOM) in the natural environment, which may greatly alter their surface properties. For example, C_{60} that is hydrophobic can be shifted to hydrophilic by surface hydroxylation by means of oxidation and thus hydroxylated C_{60} is more easily dispersed in water compared to pristine C_{60}, thereby resulting in different environmental fate and transport. Additionally, the adsorption of hydrophobic organics may induce appreciable hydrophobic interactions and particle aggregation.

Besides, the design and synthesis of ENPs for various applications often require specific surface coatings or functionalization, which render special surface chemistries and hydrophobicity.[19,20] For instance, hydrophobic NPs such as polymeric NPs are used for bioremediation of hydrophobic contaminants.[21] Chitosan or chitosan-DNA NPs serve as new vehicles in drug and gene deliveries.[22] Likewise, functionalized gold NPs (fGNPs) can be modified to hydrophobic in drug delivery applications to increase the delivery efficiency.[23]

Clearly, the determination of the surface hydrophobicity of NPs is challenged by aqueous environment factors and the heterogeneous properties of NPs that potentially depend on morphology (size and shape), surface charge, aggregation states, and surface sorption or coating. For example, the surface energy of nanomaterials could be dependent on size and shape,[24,25] surface structures,[26] and lattice parameters.[27] During the last few decades, intensive efforts have been made to develop experimental methods to accurately determine local surface hydrophobicity of NPs. Reported methods that are used to probe nanomaterial hydrophobicity include the measurements of water contact angle, octanol–water partition coefficient (K_{ow}) and surface adsorption of probe molecules.[28]

1.3. Current characterization methods for nanomaterial hydrophobicity and their limitations

(1) Contact angle measurement. Contact angle measurement (CAM) has long been used as a criterion of the static hydrophobicity of solid surfaces. It is a simple-to-adopt method for surface hydrophobicity analysis based on the sessile drop Young–Laplace method. Surfaces with small water contact angles ($<30^\circ$) are usually called hydrophilic surfaces, while for contact angles higher than 90°, the surface is considered as hydrophobic. The water contact angle reflects an average hydrophobicity of macroscale flat solid surfaces. Kuna *et al.*[26] found that the local hydrophobicity may be influenced by the nanoscale features of the materials and thus the bulk water contact angles may not directly indicate local surface hydrophobicity of individual NPs at the liquid interface.

Contact angles (CA) exhibit dependence on the position of liquid drops on heterogeneous material surfaces.[29,30] For example, the contact angle measurement could be influenced by surface roughness, surface contamination or coating and the gas pocket trapped in the interparticle void space on the film (lotus effect).[31,32] One example is that a perfectly pure gold surface is hydrophilic but due to carbon contamination in the crystal lattice most gold surfaces appear to be slightly hydrophobic.[33] Because NPs tend to interact with NOM (*e.g.*, humic acid and fulvic acid), proteins and salts in the environment,[34,35] the typical surface groups on NPs may include $-NH_2$, –OH and –COOH as well as common cations and anions (*e.g.*, Na^+, Ca^{2+}, Cl^- and SO_4^{2-}). Thus, most metallic and metal oxide NPs in the environment should be close to hydrophilic.

Although microscopy has been utilized to measure localized water contact angles on the sample surface,[36] high-resolution nanoscale visualization of liquid drops has still not been achieved. To tackle this problem, a gel trapping technique (GTT) was developed to determine the contact angles of individual colloidal particles at liquid surfaces.[37,38] As illustrated previoulsy,[37] NPs were trapped at the surface of an aqueous gel, molded with curable poly(dimethylsiloxane) (PDMS), which was lifted up and imaged with a high-resolution camera to determine the contact angles at the air–water or oil–water interface. In addition, SEM, X-ray microscopy, confocal microscopy and atomic force microscopy (AFM) have been applied to assist the visualization of local contact angles.[37,39,40] In practice, it is difficult to measure the contact angle accurately for colloidal particles, because the particle surface and the interface are optically unclear. Besides, the GTT method requires complicated sample preparation, which introduces uncertainties or artifacts.

(2) Partition coefficient (K_{ow}) measurement. Some studies proposed employing the octanol–water partitioning coefficient (K_{ow}) to represent the surface hydrophobicity of NPs.[41–43] K_{ow} is typically defined as the mass ratio of a molecular concentration in the octanol phase to its concentration in water. This ratio reflects the partitioning affinity of the tested molecules to the organic phase. A high K_{ow} generally indicates that the chemical molecules have high tendency to partition into organic phases and may show greater potential to enter and accumulate in biological interfaces. For example, DDT (di(*para*-chlorophenyl)-trichloroethane) or dioxins are hydrophobic pollutants that have high K_{ow} values. However, the theoretical basis of K_{ow} is established on molecular partitioning processes that the tested substances can diffuse between water/organic phases, which is not applicable for insoluble NPs or nanomaterials.[28,44] Also, the NPs render different processes, such as transport, aggregation and accumulation at phase interfaces, which make it impossible to achieve the thermodynamic conditions for an equilibrium

distribution of nanomaterials. Thus, partitioning experiments can hardly reflect the real hydrophobicity properties of individual NPs and may lead to erroneous predictions of environmental fate.[44] Finally, partitioning coefficients render no information on nanoscale material hydrophobicity.

(3) Hydrophobic or hydrophilic probe molecule method. The surface adsorption of different hydrophobic or hydrophilic probe molecules (*e.g.*, *p*-xylene, chlorobenzene, naphthalene and phenol) was reported to evaluate the relative hydrophobicity/hydrophilicity of nanomaterials.[28,45–47] Briefly, the quantities of the probe molecules absorbed on nanomaterial surfaces and in the media are measured at equilibrium to obtain the adsorption coefficients. The plot of adsorption coefficients against the total particle surface area yields a straight line, where the slope of the line was taken as the measure of surface hydrophobicity/hydrophilicity. If the probe compounds are hydrophobic, the larger the slope, the more hydrophobic the nanomaterials are. If the probe molecules are hydrophilic, the larger the slope, the less hydrophobic the particle is.[28,47] This method has been used to measure the surface hydrophobicity of microparticles that enable the targeted intracellular delivery of therapeutics.[48] Although this method is demonstrated well on nanomaterials of all sizes, it potentially yields misleading information due to the inherent heterogeneous and dynamic characteristics of NPs in the aqueous phase. For instance, adsorption kinetics and equilibrium are highly sensitive to and dependent on the available surface areas of NPs, which may be prone to aggregation and have reduced surface area for adsorption. Moreover, aggregation kinetics could become more complicated and unpredictable in the presence of the added hydrophobic or hydrophilic probe molecules. Moreover, the adsorption modes (Langmuir or Freundlich) of probe molecules on NPs are difficult to determine. Fang *et al.* measured the surface energy of NPs by monitoring the adsorption capacity for water molecules from the surrounding vapor, which is similar to the Brunauer, Emmett, and Teller (BET) technique for surface area measurements.[49] However, the adsorption saturation on NPs is hard to determine because of the potential multiple layered deposition of water or other molecules on the surface of NPs.

1.4. Applications of scanning-probe methods with AFM

AFM has been proven useful in the assessment of a suite of surface properties including hydrophobicity at both the microscale and nanoscale, such as soil particles,[50] microbial cells,[51] polymeric membranes,[52] and nanostructured surfaces/thin films.[31,53,54] These previous studies showed that the interfacial force measurement on AFM is shown to reveal surface energies[55] and hydrophilic or hydrophobic characteristics of the interacting surfaces.[54] AFM utilizes a sharp tip (*e.g.*, 10–15 nm radius of curvature) to measure the adhesion force that arises from adhesive bonds between the two interacting surfaces.[25] Based on the continuum thermodynamic approach (CTA), adhesion energy is related to the macroscopic observations of contact angles (*e.g.*, the Young–Dupré equation) and potentially renders hydrophobicity of the probed sites.[26,51] Noel *et al.* also found that the adhesion force measured between AFM tips and self-assembled monolayers (SAMs) of different functional groups (*e.g.*, methyl, ester and amine) increased linearly with the surface energy determined with contact angles.[56] For nanomaterials, it remains elusive if such a correlation or agreement exists between adhesion energy and water contact angle. Clearly, a direct correlation will allow us to better probe nanoscale surface hydrophobicity and crystallographic orientation or facet-dependent surface energy of nanocrystals.[57,58]

1.5. Relationship between adhesion work and hydrophobicity

To engage the AFM probe tip to contact a sample surface, external work is applied to expel solvent or water molecules that adsorb on both the tip and sample surfaces. Once in contact, the functional groups of probe tips and sample surfaces will establish hydrogen bonding or other adhesive bonding. To break up the contact, the tip will be pulled to overcome the adhesion force (F_{ad}) as shown in Fig. 1a and adhesion energy (W_{ad}). W_{ad} can be obtained by the integration in the force–distance curve ($W_{ad} = \int F_{ad} dZ$, where Z is the interaction distance) as shown in the triangle gray area in Fig. 1a. W_{ad} is related to the model of Johnson, Kendall, and Roberts (JKR model) by:

$$\frac{W_{ad}}{\pi \cdot a^2} = \frac{F_{ad}}{1.5\pi \cdot R_c} = \gamma_L - \gamma_L \cdot \cos\theta_{SL} \quad (1)$$

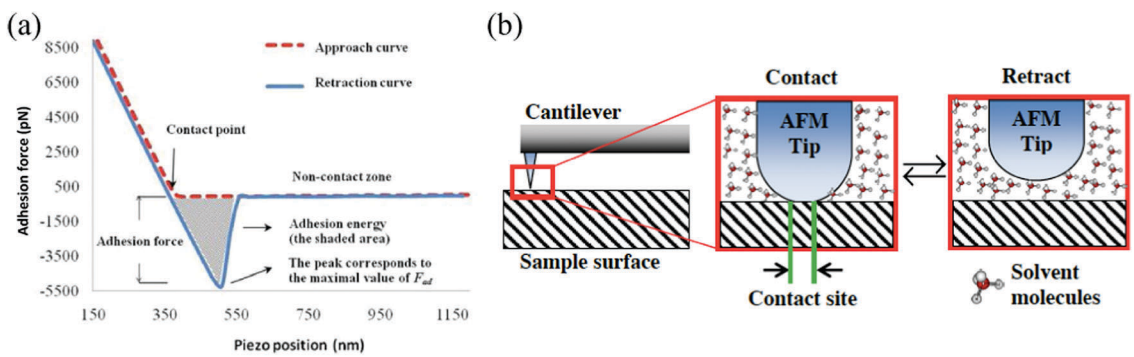

Fig. 1 (a) Representive force–distance curve from which adhesion force (F_{ad}) and adhesion energy (W_{ad}) were calculated. (b) Scheme of adhesion force measurement with AFM and the Asakura–Oosawa theory employed to calculate the free energy changes between the contact and retraction states of the AFM tip against the sample surface.

where W is the adhesion energy per unit contact area in the JKR equation, F_{ad} is the adhesion force, R_c is the radius of curvature for the cantilever tip (nm) that is determined by SEM, and a is the contact site radius. Thus, the adhesion energy is equal to the increase of surface energy in the red box in Fig. 1b after the tip is pulled up:[59]

$$W_{ad} = (\gamma_{SL} + \gamma_{TL} - \gamma_{TS})\cdot\pi\cdot a^2 \quad (2)$$

where γ_{SL}, γ_{TL} and γ_{TS} are the interfacial energies between the sample surface and liquid interfaces, between the tip surface and liquid interfaces, and between the tip and sample surface, respectively (mJ m^{-2}). Eqn (2) is supported by the depletion attraction mechanism in the Asakura–Oosawa theory,[60] which indicates that when the two surfaces come into contact, water molecules are stripped from the interspace and water molecules outside the two surfaces will exert pressure on the two contact bodies, which enhances the attraction between the two surfaces as shown in Fig. 1b. The free energy is released when the two surfaces come into contact because of the changes and reconstruction of surface energy (solvation layers).[60] According to the Dupré equation, γ_{SL}, γ_{TL} and γ_{TS} can be further expressed as:

$$\gamma_{SL} = \gamma_S + \gamma_L - W_{SL} \quad (3)$$

$$\gamma_{TL} = \gamma_T + \gamma_L - W_{TL} \quad (4)$$

$$\gamma_{TS} = \gamma_T + \gamma_S - W_{TS} \quad (5)$$

Eqn (3) and (4) indicate that the interfacial energies are directly linked to solid (sample and tip) and liquid solvent surface energies (γ_S, γ_T and γ_L) and the work of adhesion (W_{SL}, W_{TL} and W_{TS}).[26] W_{SL} can be deduced from the water contact angle using Young's equation:

$$W_{SL} = \gamma_{LV}(1 + \cos\theta_{SL}) \approx \gamma_L(1 + \cos\theta_{SL}) \quad (6)$$

where γ_{LV} is the interfacial energy between the liquid and vapor interface (mJ m^{-2}), θ_{SL} and θ_{TL} are the contact angles between the probe liquid and sample and tip surfaces. W_{TL} is equal to W_{TS} if the tip only involves London dispersion interactions with the solvent molecules or sample surfaces.[51] Combining eqn (2)–(6) yields the relationship between W_{ad} and contact angles:

$$W_{ad} = (\gamma_S - \gamma_L\cos\theta_{SL} + \gamma_T - \gamma_L\cos\theta_{TL})\cdot\pi\cdot a^2 \quad (7)$$

Eqn (7) can be converted to an adhesion force-based form according to the JKR model:

$$W = \frac{W_{ad}}{\pi a^2} = \frac{F_{ad}}{1.5\pi R_c} \quad (8)$$

Eqn (8) indicates that the adhesion force (F_{ad}) is linearly related to the contact angle (θ_{SL}) and the surface tension of probe liquids (γ_L). Thus, by measuring the adhesion force, we can quantitatively and precisely measure the local contact angle (θ_{SL}) at the resolution of the contact site area ($\pi\cdot a^2$). In contrast, the traditional contact angle measurement of θ_{SL} is a measure of macroscopic surface hydrophobicity of the bulk materials. Besides, the relation in eqn (7) or (8) is a more generalized form than that proposed by Alsteens *et al.*,[51] who only derived the relation for CH_3-modified tip and CH_3-/OH-modified sample surfaces. Eqn (7) or (8) is applicable for different tip–sample interactions and enables us to probe the surface hydrophobicity at the nanoscale. The following sections will experimentally verify the applicability of eqn (7) or (8) by testing different self-assembled monolayer (SAM) surfaces with known contact angles and further on seven different NPs.

To overcome the sizable limitations of the conventional measurement of surface hydrophobicity for nanomaterials, this study demonstrated a scanning-probe method with atomic force microscopy (AFM) to accurately determine local surface hydrophobicity through the measurement of the adhesion force between functionalized AFM probe tips and the sample surface. The adhesion force was then converted to contact angle values (''nanoscale water contact angles''). In our study, four types of hydrophilic or hydrophobic self-assembly monolayers (SAMs), namely, polyethylene glycol (PEG), biotin, streptavidin, and silane, were used to create ultra-smooth and well-ordered structure surfaces that warranted homogeneous tip–sample interactions. Different NPs including CeO_2, hematite (α-Fe_2O_3), TiO_2, ZnO, CuO, SiO_2, Ag, C_{60}, and multiwalled carbon nanotubes (MWCNTs) were prepared and immobilized on a silicon substrate and then probed by chemically functionalized AFM tips. Adhesion forces were also assessed at different solution pH, ionic strength (IS), and the presence of NOM.

2. Experimental

2.1. NPs and characterization

All NPs were purchased from commercial sources as summarized in Table S1 in the ESI.† Water suspensions of different NPs (*i.e.*, TiO_2, ZnO, SiO_2, CuO, CeO_2, α-Fe_2O_3, and Ag with citric acid coating) were made by dispersing the powers into deionized (DI) water (Millipore, 18.2 MΩ). The NP suspension was sonicated (Misonix sonicator S-4000, Qsonica, LLC). The NPs were immobilized on clean and flat silicon undoped (N-type) wafer surfaces with surface orientation (100) *via* spin-coating on a spin coater device (Laurell WS-400E). The silicon wafer was cleaved into small pieces of about 3 mm × 8 mm. They were immersed in 2% ultrapure nitric acid solution for 30 min and then 90% high purity ethanol was used to rinse it rigorously. Finally, DI water was sprayed onto the silicon surface to remove any residual impurities on the surface and place the clean silicon chips in a Petri dish. A typical thin layer of NPs was achieved by dropping 200 μL of the NP suspension with a mass concentration of approximately 100 mg L^{-1} on the substrate and spun at 3000 rpm for 5 min. Finally, samples were air dried for 5–10 min before measuring water contact angles. The morphology and sizes of NPs were determined by transmission electron microscopy (TEM, Philips EM420) at 47–120 kV. The hydrodynamic diameters of NPs were determined using a dynamic light scattering (DLS) instrument (Nano ZS Zetasizer, Malvern Instruments).

To ensure the tip–sample interactions in AFM force measurement, a full surface coverage of deposited NPs on the substrate surface must be achieved. However, the depth of the deposited

NPs (in the multilayer or the monolayer) is not controlled and does not likely affect the adhesion force measurements, because the adhesion force is measured on the outer surface of the deposited NP layers (the inner or deeper surface of layered NPs is not accessible by AFM probes).

2.2. Preparation of the SAM substrate surface

To establish a linear correlation between adhesion force and water contact angle, we measured the adhesion forces between AFM tips and alkanethiol SAMs terminated with –OH and $–CH_3$ groups in DI water.[51] Briefly, gold-coated silicon (100) wafers were immersed in ethanol solutions containing 1 mM $HS(CH_2)_{11}CH_3$ (CAS No. 112-55-0, Sigma-Aldrich) and $HS(CH_2)_{11}OH$ (CAS No. 73768-94-2, Sigma-Aldrich) in various proportions (*e.g.*, 0 : 100–100 : 0) for 14 h and then rinsed with ethanol before use. In addition, four other SAMs including PEG, hydrophobic silane, biotin, and biotin–streptavidin conjugates (MicroSurfaces Inc. USA) were coated on 2 × 2 cm glass slides to verify the correlation. Water contact angles were measured on these functionalized substrate surfaces with a Model 250 Ramé-hart goniometer under ambient conditions.

2.3. Functionalization of AFM probe tips

Two kinds of AFM cantilevers were used in the experiments to compare the coating effects on adhesion force measurements. One was gold-coated silicon nitride (Si_3N_4) cantilevers (RC800PB, Asylum Research, USA), and the other was non-coated Si_3N_4 cantilevers (MCLT, Veeco, USA). Before the functionalization, the tips were rinsed with deionized water and then methanol to remove any surface contaminants from probes. Hydrophobic cantilevers were obtained by functionalizing the gold-coated Si_3N_4 cantilevers with $–CH_3$ groups following the same method as described in our previous work.[52] The detailed information on all the cantilevers is summarized in Table S2 (ESI†).

2.4. Adhesion force measurement with AFM

First, the adhesion force between the modified tip and the surfaces of mixed self-assembled monolayers (SAMs) of CH_3- and OH-terminated alkanethiols was measured in DI water according to the method of Alsteens *et al.*[51] The hydrophobicity of the SAM surfaces was varied due to the different molar fractions of CH_3-alkanethiols present on the gold surface (100% CH_3-terminated alkanethiols are the most hydrophobic while 100% OH-terminated alkanethiols are the most hydrophilic). The measured adhesion forces were plotted *versus* the corresponding molar fraction of CH_3-alkanethiols.

The immobilized NPs on the silicon wafer were rinsed with DI water to remove any loosely bonded NPs and then placed in a liquid cell containing DI water or other desirable solutions for at least 15 min before the adhesion force measurement. Sample images were first acquired by AFM at scanning speeds varying from 2000–5000 nm s^{-1}, depending on the image quality. The AFM probe tips were engaged onto the NP surfaces at least 50–70 different locations to collect the force–distance curves and generate a histogram of adhesion force distribution for each sample (Fig. S2 and S3, ESI†). Detailed operation of AFM in the force mode and the quality check procedure are provided in Sections S2 and S3 in the ESI.†

2.5. The effects of ionic strength, pH and NOM on the hydrophobicity of MWCNTs and C_{60}

The pH of the MWCNT or C_{60} solutions was adjusted to 3.5, 7.0, and 9.0 by 0.1 M NaOH or 0.1 M HCl while the ionic strength of the suspension after the adjustment was less than 10 mM to minimize the ionic strength effect on surface states or charges of NPs. When studying the effect of ionic strength, the solution pH was maintained at 6.0 ± 0.2 while the ionic strength was varied from 0.01, 0.025, 0.05, 0.075, to 0.1 M by adding KCl. MWCNTs or C_{60} were immobilized on a silicon wafer by air drying a drop of the suspension, which were then placed in the above liquid cell containing the solution of different pHs or ionic strengths for 15 min to reach the steady state or equilibrium of ion adsorption on NPs. Finally, the force measurement was conducted on the AFM following the same procedure as described in Section 2.4.

To study the NOM effect, humic acid (HA, Sigma) was prepared in DI water (600 mg L^{-1}) with overnight stirring in the dark. The solution was then filtered under vacuum using a 0.22 μm membrane filter (Whatman), adjusted to pH 6.0 ± 0.2, and subsequently stored in the dark at 4 °C. To achieve sufficient surface coating or adsorption of humic acid on MWCNTs or C_{60}, 100 μL of the NP suspension was mixed with 200 μL of the humic acid stock solution, followed by vortexing (Mini Vortexer, Fisher Scientific) to homogenize the suspension.[61] The mixture suspension was left in the dark for 2 h to permit adsorption equilibrium, followed by centrifugation at 10 000 × *g* for 5 min to settle the NPs from water. After the supernatant was discarded, NPs were resuspended by DI water and rinsed twice to remove loosely bound humic acid on the surface of NPs. The humic acid-adsorbed NPs were then deposited on the silicon wafer for the AFM analysis.

2.6. Statistical analysis

The measured contact angles were obtained with at least triplicate sampling and testing. The calculated contact angles with adhesion forces were obtained with 50–70 force curves. The presented results are mean values ± standard deviation. The differences between calculated and measured contact angles, and the differences between test groups were tested for significance using the *t*-test at a significant level of 0.05.

3. Results and discussions

3.1. Water contact angles on the surfaces of NPs

Tables S3 and S4 (ESI†) summarizes the water contact angles for different NPs, gold surfaces coated with different amounts of $–CH_3$ groups and different SAM surfaces. The surface hydrophobicity follows an order of TiO_2 > Fe_2O_3 > CuO > CeO_2 > SiO_2 > ZnO > AgNPs coated with citric acid. When the advancing water contact angle (θ) on the surface is less than 15°, the hydration force becomes significant and stabilizes the

colloidal suspension, which explains the stable dispersion of TiO_2 or Fe_2O_3 NPs. By contrast, hydrophobic forces become appreciable when $\theta > 64^\circ$ and particle aggregation may take place.[62]

3.2. Adhesion force measurement between functionalized tips with different surface functionalization and SAMs

Our results in Fig. 2a indicated that adhesion forces for different tips all increased as the molar fraction of CH_3-alkanethiols increased, which is consistent with the previous literature.[26,51] Compared to the gold tip coated with CH_3 ligands, the bare gold tips and Si_3N_4 tips also yielded a similar dependence but a lower level of adhesion force. Moreover, the plots of adhesion forces and the values of $-\cos(\theta_{SL})$ showed good linearity in Fig. 3b–d, which matches our model relation in eqn (8). The linear fitting for the CH_3-gold tip led to a correlation coefficient of 0.98, higher than those of bare gold tips or Si_3N_4 tips.

The adhesion forces between the three types of AFM tips and four different SAM surfaces are shown in Fig. 3a. Fig. 3b and c shows the linear curve fitting for adhesion forces *versus* the values of $-\cos(\theta_{SL})$. The two uncoated AFM tips, however, yielded poorer linearity as indicated by the fluctuations of adhesion forces on the hydrophilic SAM surfaces (*e.g.*, PEG, biotin, and streptavidin). Previous work indicated that the correlation between the adhesion force and surface energy is the highest for the $-CH_3/-CH_3$ molecules on the interacting surfaces,[63] compared to other interacting molecular groups (–COOH/–COOH, $-CH_3$/–COOH, $-CH_3$ or –COOH/octenyl-trichlorosilane). This supports our results that $-CH_3$ coated gold tips yielded a strong linear dependence on adhesion force and negative cosine of water contact angles.

According to eqn (8), the linear equation should have a slope equal to the surface energy of water (γ_L), which is 72.8 mJ m^{-2} or 0.0728 N m^{-1} at 25 °C. This is close to the slope (0.10 N m^{-1}) fitted from the data for SAM surfaces in Fig. 3b. However, the experimentally fitted slope may vary slightly due to surface interaction characteristics.[64,65] For example, in addition to hydrophobic interactions, other non-specific binding and molecular anchoring may also contribute to surface adhesion, which explains the discrepancies of the fitted slope values from the surface energy of water (γ_L).

3.3. Adhesion force measurement between the CH_3-coated gold tip and different NPs

To calculate water contact angles from adhesion forces, we employed the linear equation in Fig. 3b as the "calibration equation". Fig. 4 shows that the contact angles calculated from adhesion forces were almost equal to the experimental measurements of bulk water contact angles for TiO_2, ZnO and CuO NPs. However, some subtle discrepancies ($p < 0.05$) existed for Fe_2O_3, CeO_2, SiO_2, and AgNPs, probably due to the effect of hydration on interfacial energy at the nanoscale.[26,66] According to Chiu *et al.*,[66] a local hydration effect can be caused by the curvature of the particle–water interface such that the surface hydrophobicity may shift from hydrophobic for ultra-small NPs to hydrophilic properties for large particles. Our previous study examined the nanoscale

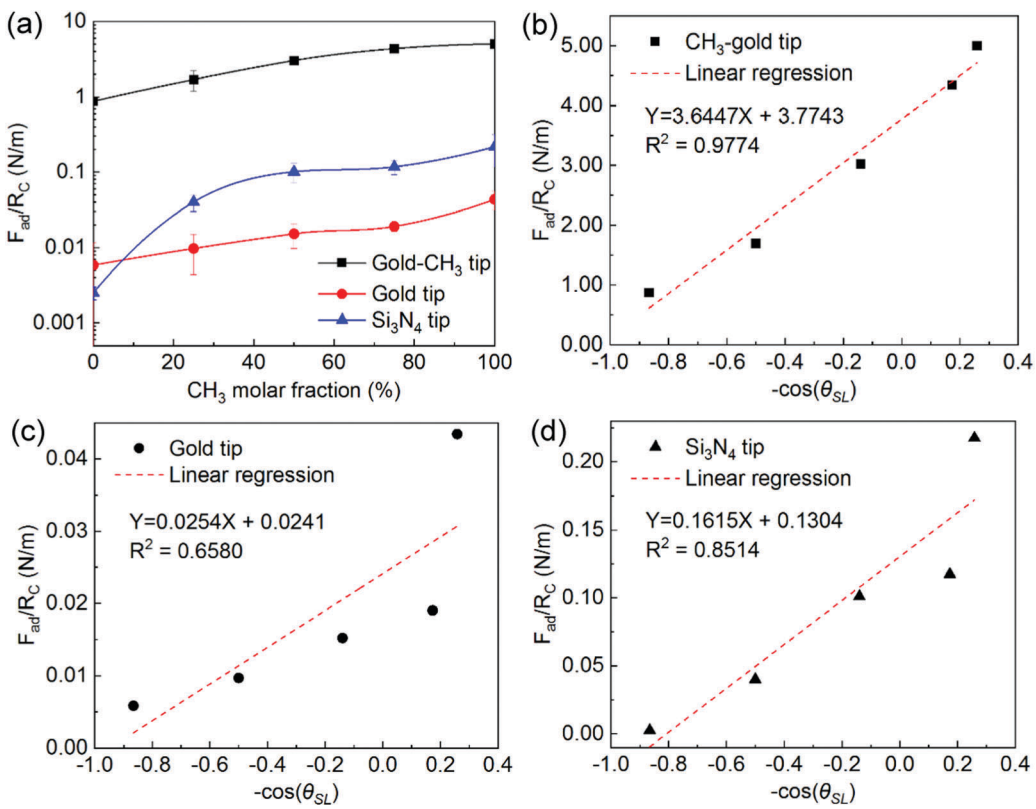

Fig. 2 (a) Adhesion force as a function of the surface fraction of CH_3-terminated alkanethiols. (b)–(d) The linear curve fitting for the results of F_{ad}/R_c and $-\cos(\theta_{SL})$ for gold tips w/o $-CH_3$ coating and the uncoated Si_3N_4 tip.

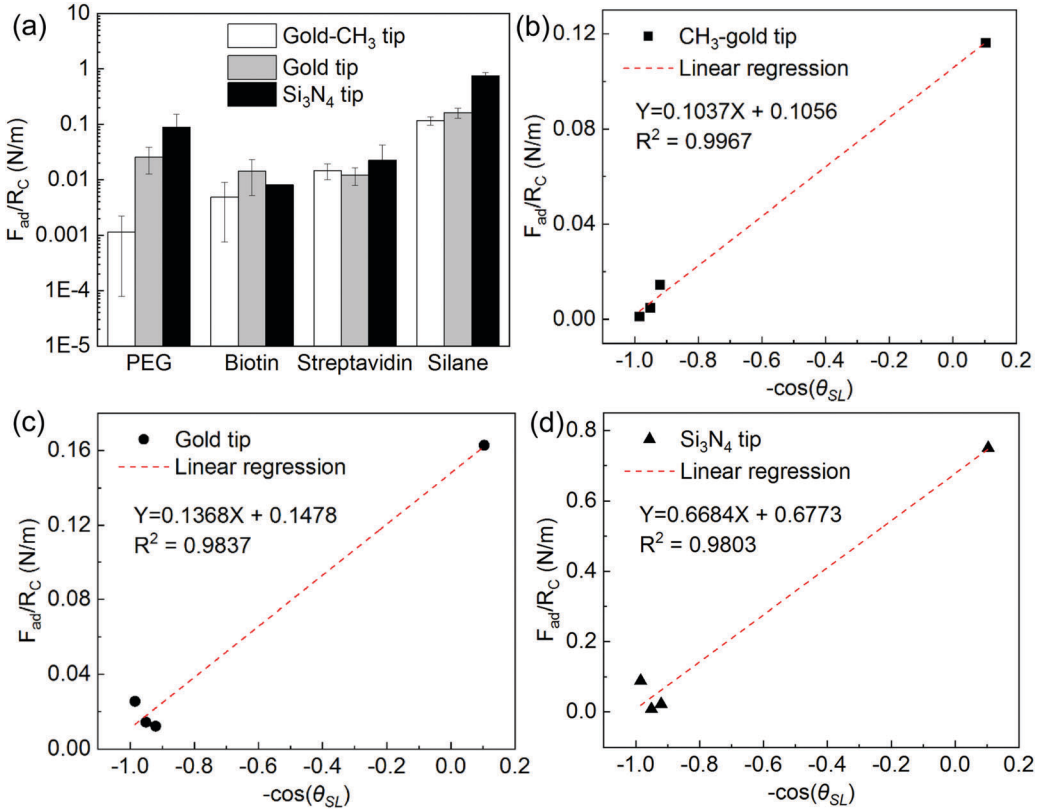

Fig. 3 (a) Adhesion forces between three types of tips and different SAM surfaces. (b)–(d) Adhesion forces *versus* the value of $-\cos(\theta_{SL})$ for three types of tips.

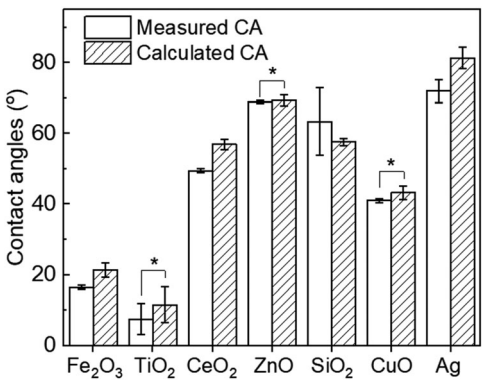

Fig. 4 Comparison between calculated and experimental contact angles for seven kinds of NPs. * indicates no significant difference ($p > 0.05$).

hydrophobicity of chemically modified polyethersulfone membranes and also found this subtle discrepancy between the bulk water contact angle and that experimentally derived from adhesion forces, which was attributed to the surface roughness effect or the lotus leaf effect.[52]

3.4. Effects of water chemistries and surface coating on the hydrophobicity of MWCNTs and C_{60}

MWCNTs and C_{60} were used as model hydrophobic nanomaterials to evaluate the effects of the solution pH, IS, and NOM on the adhesion force measurement or the surface hydrophobicity of nanomaterials. Fig. 5 shows that MWCNTs were characterized to be super-hydrophobic (the bulk water contact angles were *ca.* 150°) and C_{60} was hydrophobic (the bulk water contact angle was *ca.* 120°), which was consistent with the previous studies.[67,68] Our results indicate that pH had little influence on the measured and calculated CAs from adhesion forces on MWCNTs (Fig. 5a and b). The average measured CAs for MWCNTs were ~146° over the pH range (3.5–9.0), while the calculated CAs decreased slightly from ~170° to ~130°. Similarly, no significant differences were found between the measured CAs for C_{60} at different pHs. Meanwhile, the calculated CAs for C_{60} increased from 72° to 90° when the pH increased from 3.5 to 9.0. Different from MWCNTs, significant differences ($p < 0.05$) between the calculated and measured CAs were observed for C_{60} over the pH range (3.5–9.0), suggesting that the deposition of C_{60} on the silica surface was not homogenous at the bulk scale and nanoscale. It is reported that the deposition of the C_{60} NPs on the silica surface was mostly irreversible and C_{60} NPs may detach at high solution pHs.[69] Thus, the bulk CA measurement may likely include silicon wafer surfaces without C_{60}, especially when the pH was high (pH = 9.0). Nevertheless, this AFM probe method directly probes the surface of NPs and thus can apparently avoid potential artifacts from the sample displacement.

Fig. 5c shows no significant differences between the calculated and measured CAs, regardless of the ionic strength variations, indicating that there was a negligible effect of ionic strength on the hydrophobicity of MWCNTs. Though a decrease in the measured

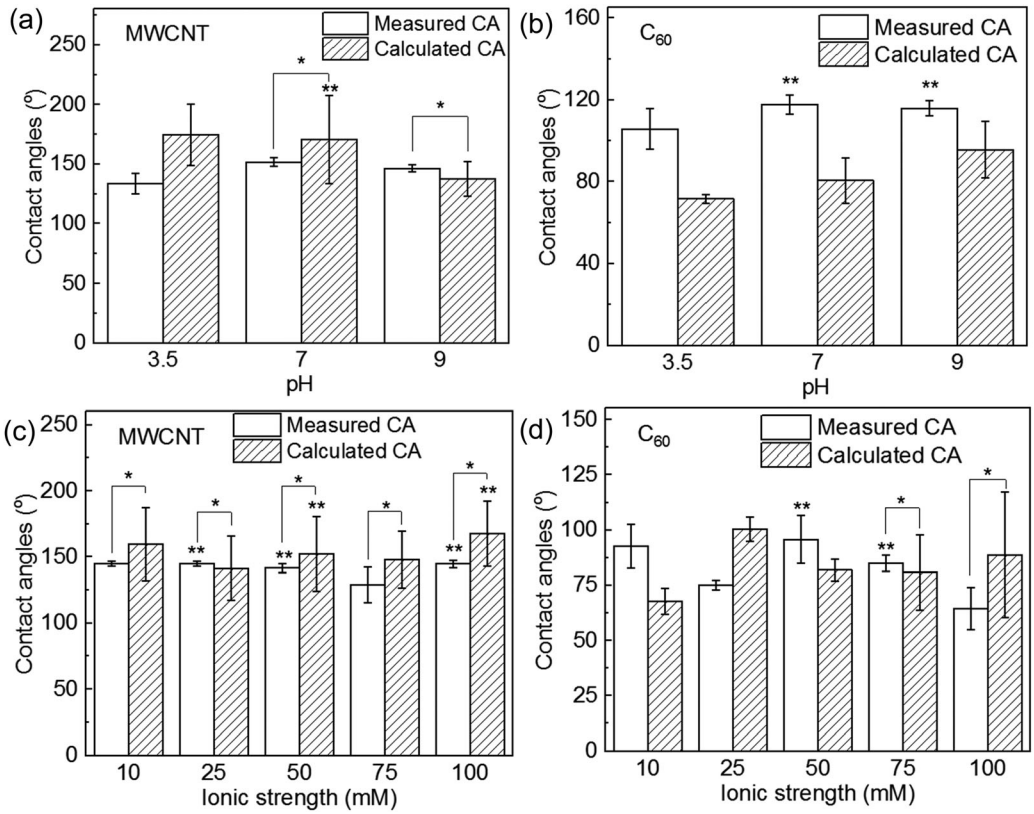

Fig. 5 Effects of pH (a and b) and ionic strength (c and d) on the contact angle measurements of C_{60} and MWCNTs. * indicates no significant difference ($p > 0.05$) between the measured and calculated contact angles. ** indicates no significance in comparison to control groups ($p > 0.05$). Control group: pH = 3.5 or IS = 10 mM.

CAs and an increase of the calculated CAs of C_{60} were observed when the ionic strength increased from 10 mM to 25 mM, there was no clear dependence for contact angles on ionic strength. The effects of pH and IS on the hydrophobicity of MWCNTs and C_{60} are negligible probably because hydrophobic MWCNTs and C_{60} had low surface interactions such as sorption of charged ions on MWCNTs or C_{60}.[70] Though many previous studies reported the effects of pH and ionic strengths on the aggregation behaviors of MWCNTs or C_{60} NPs, there was no report on hydrophobicity impacts from the changing pH or IS. It is reported that the surface tension and the contact angle of hydrophobic ethyl cellulose NPs at the interface all remain unchanged at different ionic strengths,[71] which supports our observation that hydrophobic interactions among NPs are insensitive to the solution IS.

Fig. 6 shows that the coating of HA substantially decreased the hydrophobicity of MWCNTs and C_{60} as indicated by the decrease of water contact angles, which has commonly been reported in the literature.[72–74] Due to the hydrophobic effect induced by the aliphatic components of HA, they could adsorb on carbonaceous materials (*e.g.*, MWCNTs) *via* π–π interaction, hydrogen bonding or Lewis acid–base interactions,[75–77] which ensured a stable and repeatable AFM analysis. After adsorption of HA, MWCNTs and C_{60} presented hydrophilic surfaces due to the hydrophilic domains in the HA molecule. By contrast, the coating or surface deposition of HA on metal or metal oxide NPs may change due to dissolution and results in potential

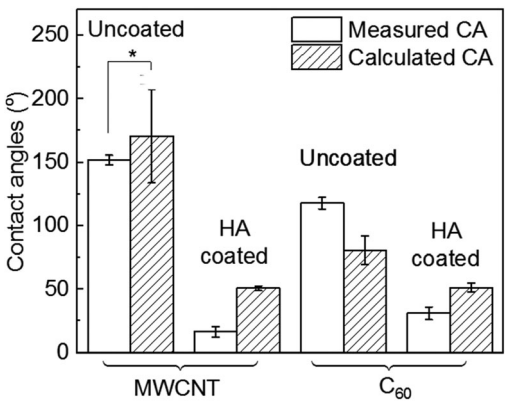

Fig. 6 Effects of HA coating on the contact angle measurements of C_{60} and MWCNTs. * indicates no significant difference ($p > 0.05$) between the measured and calculated contact angles.

discrepancies of adhesion force measurements. Nevertheless, with the surface coating by HA, we believe that the hydrophobicity shift for metal/metal oxide NPs should be similar to the results obtained for MWCNTs and C_{60} as the adhesion force is primarily contributed by tip–HA interactions.

On the other hand, obvious discrepancies between the calculated and measured CAs were observed for HA coated carbon-based nanomaterials and the measured CA was smaller than the calculated ones. This could be attributed to the uneven

adsorption of HA on nanomaterials, making some of the local surfaces of MWCNTs or C_{60} remain uncoated or partially coated, which thus exhibited a higher level of hydrophobicity. This also implies that the AFM-based method for hydrophobicity probing may reveal higher resolution and greater accuracy for nanomaterial characteristics.

4. Conclusions

The accurate characterization of nanomaterial hydrophobicity is critical for modeling and predicting the fate and transport of NPs, including aggregation, adsorption, deposition, and biological interactions. Undoubtedly, this presented scanning probe method provides an unparalleled and stable approach to evaluate the authentic hydrophobicity of nanomaterials at the nanoscale, which are different from the conventional methods. The findings unravel new insights that localized surface heterogeneity (*e.g.*, roughness, surface hydration and coating) of nanomaterials could make their nanoscale surface hydrophobicity differ from macroscopic surface hydrophobicity as commonly indicated by water contact angles. This study opens up new opportunities for exploring the heterogeneous characteristics of nanomaterials under environmentally relevant conditions.

Conflicts of interest

There are no conflicts to declare.

Acknowledgements

The authors gratefully acknowledge funding support from the NSF (Award ID: 1235166 and 1756444).

References

1 M. Kalive, W. Zhang, Y. Chen and D. G. Capco, *Cell Biol. Toxicol.*, 2012, **28**, 343–368.
2 K. Li, Y. Chen, W. Zhang, Z. Pu, L. Jiang and Y. Chen, *Chem. Res. Toxicol.*, 2012, **25**, 1675–1681.
3 Y. Li, J. Niu, W. Zhang, L. Zhang and E. Shang, *Langmuir*, 2014, **30**, 2852–2862.
4 Y. Li, W. Zhang, J. Niu and Y. Chen, *ACS Nano*, 2012, **6**, 5164–5173.
5 W. Zhang, Y. Li, J. Niu and Y. Chen, *Langmuir*, 2013, **29**, 4647–4651.
6 G. Sonavane, K. Tomoda, A. Sano, H. Ohshima, H. Terada and K. Makino, *Colloids Surf., B*, 2008, **65**, 1–10.
7 J. J. Faust, W. Zhang, B. A. Koeneman, Y. Chen and D. G. Capco, *Part. Fibre Toxicol.*, 2012, **9**, 42.
8 J. J. Faust, W. Zhang, Y. Chen and D. G. Capco, *Cell Biol. Toxicol.*, 2014, **30**, 31–53.
9 R. D. Handy, R. Owen and E. Valsami-Jones, *Ecotoxicology*, 2008, **17**, 315–325.
10 C. Peng, W. Zhang, H. Gao, Y. Li, X. Tong, K. Li, X. Zhu, Y. Wang and Y. Chen, *Nanomaterials*, 2017, **7**, 21.
11 H. Y. Kim, J. O. Sofo, D. Velegol, M. W. Cole and A. A. Lucas, *Langmuir*, 2007, **23**, 1735–1740.
12 Y. Li, X. Chen and N. Gu, *J. Phys. Chem. B*, 2008, **112**, 16647–16653.
13 R. Qiao, A. P. Roberts, A. S. Mount, S. J. Klaine and P. C. Ke, *Nano Lett.*, 2007, **7**, 614–619.
14 K. Kostarelos, L. Lacerda, G. Pastorin, W. Wu, S. Wieckowski, J. Luangsivilay, S. Godefroy, D. Pantarotto, J. P. Briand, S. Muller, M. Prato and A. Bianco, *Nat. Nanotechnol.*, 2007, **2**, 108–113.
15 A. Verma, O. Uzun, Y. Hu, H. S. Han, N. Watson, S. Chen, D. J. Irvine and F. Stellacci, *Nat. Mater.*, 2008, **7**, 588–595.
16 X. Feng, L. Feng, M. Jin, J. Zhai, L. Jiang and D. Zhu, *J. Am. Chem. Soc.*, 2004, **126**, 62–63.
17 H. S. Lim, D. Kwak, D. Y. Lee, S. G. Lee and K. Cho, *J. Am. Chem. Soc.*, 2007, **129**, 4128–4129.
18 B. Yan, J. Tao, C. Pang, Z. Zheng, Z. Shen, C. H. A. Huan and T. Yu, *Langmuir*, 2008, **24**, 10569–10571.
19 C. Grabinski, N. Schaeublin, A. Wijaya, H. D'Couto, S. H. Baxamusa, K. Hamad-Schifferli and S. M. Hussain, *ACS Nano*, 2011, **5**, 2870–2879.
20 A. Albanese, P. S. Tang and W. C. W. Chan, *Annu. Rev. Biomed. Eng.*, 2012, **14**, 1–16.
21 W. Tungittiplakorn, C. Cohen and L. W. Lion, *Environ. Sci. Technol.*, 2004, **39**, 1354–1358.
22 H.-Q. Mao, K. Roy, V. L. Troung-Le, K. A. Janes, K. Y. Lin, Y. Wang, J. T. August and K. W. Leong, *J. Controlled Release*, 2001, **70**, 399–421.
23 P. Ghosh, G. Han, M. De, C. K. Kim and V. M. Rotello, *Adv. Drug Delivery Rev.*, 2008, **60**, 1307–1315.
24 M. Magomedov, *Phys. Solid State*, 2004, **46**, 954–968.
25 W. Zhang, A. G. Stack and Y. Chen, *Colloids Surf., B*, 2011, **82**, 316–324.
26 J. J. Kuna, K. Voitchovsky, C. Singh, H. Jiang, S. Mwenifumbo, P. K. Ghorai, M. M. Stevens, S. C. Glotzer and F. Stellacci, *Nat. Mater.*, 2009, **8**, 837–842.
27 P. Zhou, X. Zhu, J. Yu and W. Xiao, *ACS Appl. Mater. Interfaces*, 2013, **5**, 8165–8172.
28 Y. Xiao and M. R. Wiesner, *J. Hazard. Mater.*, 2012, **215-216**, 146–151.
29 M. S. Bell, A. Shahraz, K. A. Fichthorn and A. Borhan, *Langmuir*, 2015, **31**, 6752–6762.
30 A. Deak, E. Hild, A. L. Kovacs and Z. Horvolgyi, *Phys. Chem. Chem. Phys.*, 2007, **9**, 6359–6370.
31 J. J. Kuna, K. Voitchovsky, C. Singh, H. Jiang, S. Mwenifumbo, P. K. Ghorai, M. M. Stevens, S. C. Glotzer and F. Stellacci, *Nat. Mater.*, 2009, **8**, 837–842.
32 H.-J. Butt, B. Cappella and M. Kappl, *Surf. Sci. Rep.*, 2005, **59**, 1–152.
33 T. Smith, *J. Colloid Interface Sci.*, 1980, **75**, 51–55.
34 G. R. Aiken, H. Hsu-Kim and J. N. Ryan, *Environ. Sci. Technol.*, 2011, **45**, 3196–3201.
35 M. Horie, K. Nishio, K. Fujita, S. Endoh, A. Miyauchi, Y. Saito, H. Iwahashi, K. Yamamoto, H. Murayama, H. Nakano, N. Nanashima, E. Niki and Y. Yoshida, *Chem. Res. Toxicol.*, 2009, **22**, 543–553.
36 K. M. Forward, A. L. Moster, D. K. Schwartz and D. J. Lacks, *Langmuir*, 2007, **23**, 5255–5258.

37 L. N. Arnaudov, O. J. Cayre, M. A. Cohen Stuart, S. D. Stoyanov and V. N. Paunov, *Phys. Chem. Chem. Phys.*, 2010, **12**, 328–331.
38 O. J. Cayre and V. N. Paunov, *Langmuir*, 2004, **20**, 9594–9599.
39 B. M. Weon, J. San Lee, J. T. Kim, J. Pyo and J. H. Je, *Curr. Opin. Colloid Interface Sci.*, 2012, **17**, 388–395.
40 L. Isa, F. Lucas, R. Wepf and E. Reimhult, *Nat. Commun.*, 2011, **2**, 438.
41 K. D. Hristovski, P. K. Westerhoff and J. D. Posner, *J. Environ. Sci. Health, Part A: Toxic/Hazard. Subst. Environ. Eng.*, 2011, **46**, 636–647.
42 P. Westerhoff and B. Nowack, *Acc. Chem. Res.*, 2012, **46**, 844–853.
43 W.-C. Hou, B. Y. Moghadam, P. Westerhoff and J. D. Posner, *Langmuir*, 2011, **27**, 11899–11905.
44 A. Praetorius, N. Tufenkji, K.-U. Goss, M. Scheringer, F. von der Kammer and M. Elimelech, *Environ. Sci.: Nano*, 2014, **1**, 317–323.
45 X. Xia, R. Baynes, N. Monteiro-Riviere and J. Riviere, *SAR QSAR Environ. Res.*, 2007, **18**, 579–593.
46 X. Xia, N. A. Monteiro-Riviere and J. Riviere, *Nat. Nanotechnol.*, 2010, **5**, 671.
47 Y. Xiao and M. R. Wiesner, *Environ. Sci. Technol.*, 2013, **47**, 2246–2253.
48 L. Thiele, H. P. Merkle and E. Walter, *Pharm. Res.*, 2003, **20**, 221–228.
49 X. Fang, B. Li, I. V. Chernyshova and P. Somasundaran, *J. Phys. Chem. C*, 2010, **114**, 15473–15477.
50 S. Y. Cheng, R. Bryant, S. H. Doerr, C. J. Wright and P. R. Williams, *Environ. Sci. Technol.*, 2009, **43**, 6500–6506.
51 D. Alsteens, E. Dague, P. G. Rouxhet, A. R. Baulard and Y. F. Dufrêne, *Langmuir*, 2007, **23**, 11977–11979.
52 W. Fu, C. Carbrello, X. Wu and W. Zhang, *Nanoscale*, 2017, **9**, 15550–15557.
53 K. Voitchovsky, J. J. Kuna, S. A. Contera, E. Tosatti and F. Stellacci, *Nat. Nanotechnol.*, 2010, **5**, 401–405.
54 L. Sirghi, M. Nakamura, Y. Hatanaka and O. Takai, *Langmuir*, 2001, **17**, 8199–8203.
55 T. Eastman and D.-M. Zhu, *Langmuir*, 1996, **12**, 2859–2862.
56 O. Noel, M. Brogly, G. Castelein and J. Schultz, *Langmuir*, 2004, **20**, 2707–2712.
57 S. Deshpande, S. Patil, S. V. Kuchibhatla and S. Seal, *Appl. Phys. Lett.*, 2005, **87**, 133113.
58 B. Wiley, Y. G. Sun, B. Mayers and Y. N. Xia, *Chem. – Eur. J.*, 2005, **11**, 454–463.
59 C. C. Dupont-Gillain, B. Nysten, V. Hlady and P. G. Rouxhet, *J. Colloid Interface Sci.*, 1999, **220**, 163–169.
60 D. Marenduzzo, K. Finan and P. R. Cook, *J. Cell Biol.*, 2006, **175**, 681–686.
61 K. L. Chen and M. Elimelech, *J. Colloid Interface Sci.*, 2007, **309**, 126–134.
62 W. A. Ducker and L. M. Grant, *J. Phys. Chem.*, 1996, **100**, 11507–11511.
63 S. C. Clear and P. F. Nealey, *J. Colloid Interface Sci.*, 1999, **213**, 238–250.
64 J. H. Park and N. Aluru, *Mol. Simul.*, 2009, **35**, 31–37.
65 A. Noy, S. Zepeda, C. A. Orme, Y. Yeh and J. J. De Yoreo, *J. Am. Chem. Soc.*, 2003, **125**, 1356–1362.
66 C.-c. Chiu, P. B. Moore, W. Shinoda and S. O. Nielsen, *J. Chem. Phys.*, 2009, **131**, 244706.
67 N. Francesco De, C. Paola, S. Manuela, N. Francesca, C. Ilaria and C. Maurizio De, *Nanotechnology*, 2015, **26**, 145701.
68 J. I. Choi, S. D. Snow, J.-H. Kim and S. S. Jang, *Environ. Sci. Technol.*, 2015, **49**, 1529–1536.
69 K. L. Chen and M. Elimelech, *Langmuir*, 2006, **22**, 10994–11001.
70 A. I. Frolov, A. G. Rozhin and M. V. Fedorov, *ChemPhysChem*, 2010, **11**, 2612–2616.
71 N. Bizmark and M. A. Ioannidis, *Langmuir*, 2015, **31**, 9282–9289.
72 M. A. Chappell, A. J. George, K. M. Dontsova, B. E. Porter, C. L. Price, P. Zhou, E. Morikawa, A. J. Kennedy and J. A. Steevens, *Environ. Pollut.*, 2009, **157**, 1081–1087.
73 H. Hyung, J. D. Fortner, J. B. Hughes and J.-H. Kim, *Environ. Sci. Technol.*, 2007, **41**, 179–184.
74 D. Zhang, B. Pan, R. L. Cook and B. Xing, *Environ. Pollut.*, 2015, **196**, 292–299.
75 C. Zhang, L. Wu, D. Cai, C. Zhang, N. Wang, J. Zhang and Z. Wu, *ACS Appl. Mater. Interfaces*, 2013, **5**, 4783–4790.
76 Z. Yang, H. Yan, H. Yang, H. Li, A. Li and R. Cheng, *Water Res.*, 2013, **47**, 3037–3046.
77 X. Wang, L. Shu, Y. Wang, B. Xu, Y. Bai, S. Tao and B. Xing, *Environ. Sci. Technol.*, 2011, **45**, 9276–9283.